Journal of Renewable Materials
DOI:10.32604/jrm.2020.08493
Research Article

Poly (vinyl alcohol)/Graphene Nanocomposite Hydrogel Scaffolds for Control of Cell Adhesion

Xiaodong Wang[1,2], Meng Su[2], Chuntai Liu[2], Changyu Shen[2] and Xianhu Liu[2,*]

[1]Department of Materials Science and Engineering, Tongji Zhejiang College, Jiaxing, 314051, China
[2]National Engineering Research Center for Advanced Polymer Processing Technology, Zhengzhou University, Zhengzhou, 450002, China
*Corresponding Author: Xianhu Liu. Email: xianhu.liu@zzu.edu.cn
Received: 30 August 2019; Accepted: 22 October 2019

Abstract: Poly (vinyl alcohol) (PVA)/reduced graphene oxide (rGO) nanocomposites is prepared by the immersion of PVA/graphene oxide (GO) nanocomposites in the reducing agent aqueous solution. The PVA/graphene nanocomposites can be used as scaffold after treatment by chemical crosslinking agents. The surface hydrophilicity of the nanocomposite scaffolds decreased with the addition of GO or rGO by measuring the contact angles of scaffolds. The electrical conductivity of PVA/rGO nanocomposite scaffold increased with rGO content increased. The highest conductivity of PVA/rGO nanocomposite scaffolds with 10 wt% rGO could reach to 12.16×10^{-3} S/m. The NIH-3T3 fibroblasts attach and grow well on the surface of PVA/rGO nanocomposite scaffolds with increasing the content of rGO. The number of cells obviously increases on the PVA/rGO nanocomposite scaffolds, especially, at 5 wt% and 10 wt% rGO. Furthermore, a good level of conductivity and a variation in the surface property of the PVA/rGO nanocomposite scaffolds have affected NIH-3T3 fibroblasts grow.

Keywords: Graphene; nanocomposites; hydrogels; scaffolds

1 Introduction

Tissue-engineering scaffolds have been note-worthily used in regenerative medicine such as organ regeneration, disease modelling and cybernetic organism [1-4]. Excellent tissue-engineering scaffolds are expected to mimic the native properties of load bearing (ligaments, bone, cartilage, and tendon) and electroactive (cardiac, skeletal muscle, brain, and nerve) tissues in the body. However, most of the current scaffolds do not mimic gracefully the complex structure of native tissue and provide the needed mechanical, electrical, and biology stimuli. Thus, it is pivotal to develop biomimetic artificial scaffolds that are providing a microenvironment supportive of native-like extracellular matrix (ECM) [5]. A hydrogel is a unique type of soft biomaterials available for biomimetic scaffolds to support cell function, which has been used in the field of drug delivery [6] and tissue engineering [7]. Poly (vinyl alcohol) (PVA), poly (ethylene oxide), poly (ethyleneimine), poly (vinyl pyrrolidone), and poly-N-isopropylacrylamide have been reported for preparation of hydrogel. Due to excellent biocompatibility, nontoxicity and biodegradability, PVA has been used in various pharmaceutical and biomedical applications such as contact lenses, drug delivery devices, wound dressing, orthopaedic devices, artificial

organs, especially in tissue engineering applications [8-10]. However, the conventional approaches to tailor the characteristics of hydrogel scaffold have relied on adjustments of the polymer content and crosslinking density, which may affect the nutrient transport or other properties of the hydrogel scaffolds. In this case, the nanocomposite approaches have attracted a lot of attention since it could readily modulate the properties of the hydrogel scaffolds without compromising the extracellular matrix (ECM) functions [11]. Of many nanomaterials currently used in scaffolds, the conductive nanomaterials have been synthesized to reinforce the hydrogen, which are commonly carbon-based nanomaterials, including carbon nanotubes (CNTs) and graphene [12-14].

Graphene has recently been considered as a promising candidate for biomedical application, such as drug delivery, tissue engineering, diagnostic devices, and biosensor [15-17]. Furthermore, the graphene nanocomposite can be used as an excellent nanostructured scaffolds for promoting cells adhesion and differentiation for long-term periods [18-20]. Zhang et al. [18] reported that graphene oxide (GO) coated with biopolymers or surfactant displays highly biocompatible in vivo and then was cleared from mice within one week. However, the consistent answer to cellular biocompatibility of graphene and its derivatives in biological system is not made [20-23]. It was reported that the cytotoxicity of GO and rGO is mainly due to the direct contact interaction of their extremely sharp edges with membrane of cells [24]. Both GO and rGO were found to accumulate on cell membrane surfaces and penetrate the cellular membrane as intruders, which caused the decrease of cell viability, interference with cellular function or promotion harmful cellular responses. In this situation, a promising approach emerges that nanomaterials encapsulating of rGO or GO components in a matrix could avoid rGO or GO sheets penetrating into cells at the early stage and meanwhile, modulate the properties of hydrogels [25, 26]. Therefore, the hydrogel scaffolds assisted by the nanomaterials presents a facile strategy for engineering multifunctional tissue constructs. Moreover, rGO as nanofiller not only enhances mechanical stability and confers the hydrogel with electrical conductivity.

In this study, GO and rGO were selected as nanofillers to the fabrication of the polymer composite system featuring PVA as matrix. The composite was employed to fabricate the hydrogel scaffolds by chemical crosslinking. The properties of the PVA/GO nanocomposite and PVA/rGO nanocomposite were studied. Significantly, the rGO sheets provided conductive zones, thereby enabling intercellular signalling and optimizing cell activities. Then, cell assays were conducted to investigate the biocompatibility of the hydrogel scaffolds as well as cell-scaffold interactions.

2 Experimental Section

2.1 Materials and Methods

Graphite, PVA (Mw = 89,000–98,000, 99+% hydrolyzed) and chemical agents included concentrated sulfuric acid (H_2SO_4), potassium permanganate ($KMnO_4$), hydrochloric acid (HCl), $Na_2S_2O_4$, 30% hydrogen peroxide (H_2O_2), and glutaraldehyde (25% in H_2O) were purchased from Sigma Aldrich. The materials were used directly without any further purification.

In the oxidation process, GO was prepared according to the modified Hummer's method [27-30]. Briefly, graphite (2 g) was mixed with $NaNO_3$ (1 g) and H_2SO_4 (50 ml) cooling to 0°C in an ice-bath. Then $KMnO_4$ (6 g) was slowly added into the suspension and the temperature of the suspension was controlled not exceeding 20°C. Then, the suspension was stirred at 35°C for 1 h. Next, deionized water (DI) (100 ml) was slowly added into the suspension, the temperature was raised to 98°C for 3 h. The mixture was further treated with 5% H_2O_2 (50 ml), filtered and washed with distilled water. The purified GO suspensions were then dispersed in distilled water and ultrasonicated for 15 min. The obtained brown dispersion was then subjected to centrifugation, and the precipitate was dried in the refrigeration dryer for 5 days till totally dry to be stored in the desiccation.

The GO films were prepared by film casting on the glass slides. The GO films were immersed in the reducing agent solution as same as above at 60°C for 0.5 h. The color of the GO films was changed from

yellow to gray, which indicated that the reduction was occurred, and the GO films had been turned to rGO films. The rGO films were rinsed by DI to remove the residual reducing agents and by-product. The rGO films were dried at 60°C for 2 h.

2.2 Nanocomposite Preparation

PVA/GO nanocomposites containing predetermined amount of GO (as mentioned above) were prepared as follows: PVA was added in DI water at 80°C and stirred constantly for 2 hours till completely dissolved. A predetermined weight of GO was dissolved in DI water in an ultrasonic bath for 2 hours. The predetermined content of GO in the composite films was 1, 5 and 10 wt%, respectively. The mixtures were shaken for 10 min, degassed in an ultrasonic bath for 20 min, cast into Petri dishes, and then dried at 50°C in an oven until no change could be perceived in their weights. Then the PVA/GO nanocomposites were produced. Pure PVA films were prepared as a reference following the same procedures as the aforementioned ones for preparing the nanocomposites films.

The PVA/GO film was immersed in reducing agent solution (50 mg/ml of NaOH and 15 mg/ml of $Na_2S_2O_4$) at 60°C for 1 h, and the prepared PVA/GO film was washed in distilled water until the by-product and residual reducing agents were removed. After that, the film was dried at 60°C for 5 h. The PVA/GO film was turned to PVA/rGO film.

2.3 Nanocomposite Hydrogel Scaffold Preparation

The crosslinking solution was prepared by mixing 1 g of glutaraldehyde (GA) 2.5 wt% and 1 g of 36 wt% hydrochloric acid. Samples were soaked in a cross-linking bath for 24 h. Finally, the prepared films were washed repeatedly with DI, in order to eliminate any possible GA and hydrochloric acid residuals and dried at room temperature. The PVA/GO and PVA/rGO nanocomposite hydrogels were prepared for the scaffold by chemical crosslinking method.

2.4 Characterization

Fourier transform infrared (FT-IR) spectra of the nanocomposites in ATR mode were obtained using a Thermo Fisher NICOLET iS10. Wide-angle X-ray (XRD) was conducted on a Bruker/Siemens Hi-Star two-dimensional diffractometer with a monochromatic Cu Kα point source ($\lambda = 0.154184$ nm) under a voltage of 40 kV and a current of 20 mA. Samples were scanned over the integration range of diffraction angle $2\theta = 1–50°$ at room temperature. The morphologies of the samples were observed using a LEO1530 field-emission scanning electron microscope (FE-SEM) and the accelerating voltage was 5 kV.

The resistance of the samples was measured with an electrometer (Keithley). The dc electrical conductivity for weakly conductive samples was tested by high resistance meter (Agilent 4339B, USA). For the samples with better conductive behavior, the dc electrical conductivity was measured by a four-probe method. V-source testing mode (Keithley 2400 source meter, USA) was employed to make sure that a precise voltage was applied on the two inner probes. The measured voltage was adjusted in the range from −1 to 1 V, and the corresponding current was measured and recorded across the two outer probes.

The surface water contact angles of crosslinked scaffolds were carried out on a contact angle instrument (Dataphysics OCA 15, Germany) with a video by using the sessile drop mode. The drop size was set as 10 μL. Three specimens for each group were tested to calculate the average value.

2.5 Cell Culture and Seeding on Scaffolds

Scaffolds were sterilized by exposure to UV rays for 30 min before culture [22, 31]. NIH-3T3 cells (mouse embryonic fibroblast, supplied from Wisconsin Institute for Discovery, WI, USA) were cultured in Dulbecco's modified Eagle's medium (DMEM) supplemented with10% FBS (fetal bovine serum), 1 units/mL penicillin, 1 μg/mL streptomycin, and 2 mM L-glutamine at 37°C at 5% CO_2. NIH-3T3 cells were seeded on films modified with GO and rGO at a density of 10000 cells/cm^2. Cells were incubated

for 24 or 48 h and washed with sterilized PBS. Live/dead and cell number assays were taken at days 3. Three samples were tested for each group.

2.6 Live/Dead Assay

The biocompatibility of the hydrogel scaffolds was tested by examining the growth of NIH-3T3 cells via a live/dead viability/cytotoxicity assay kit (Invitrogen) after 3 days of culture. The stain utilized green fluorescent Calcein-AM to target esterase activity within the cytoplasm of living cells, and red fluorescent ethidium homodimer-1 (EthD-1) to indicate cell death by penetrating damaged cellular membranes. Stain cells were imaged with a Nikon Eclipse Ti microscope with an attached Photometrics Cool SNAP HQ2 camera. Nis-D Advanced Research v.3.22 software was used for image analysis.

3 Results and Discussion

FTIR spectroscopy is a fast and effective method for detection of various chemical bond changes in materials. Figure 1 shows the ATR-FTIR spectra of PVA and crosslinked PVA. As for FTIR analysis, the characteristic peak of the hydroxyl group (–OH) between 3000 and 3600 cm^{-1}, and the ether/acetal group (–COC or –COCO) around at 1240 cm^{-1} or 997 cm^{-1} were evaluated. The shift in intensity of –OH (decrement with the crosslinking reactions) have been a consequence of acetal interactions between the PVA and glutaraldehyde. The crosslinking reaction between the PVA chains and GA was represented by the reaction in Fig. 2. From the schematic diagram, the –OH of PVA was involved in the crosslinking reactions with GA, that resulted in a considerable reduction of the intensity of the –OH. The appearance of the ether/acetal peak indicated that the acetylation reaction occurs between aldehyde and hydroxyl groups in the polymer.

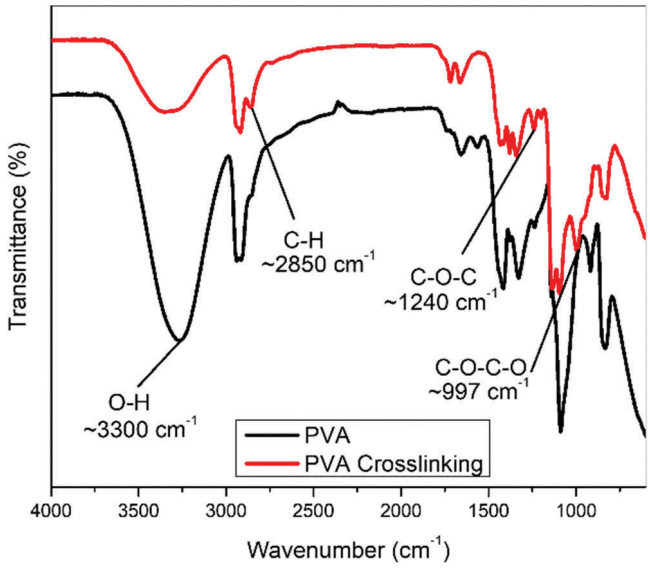

Figure 1: FT-IR spectra of PVA and crosslinked PVA films

XRD shown in the Fig. 3 was used to examine the variations of layer structure of graphite, GO, rGO, and of crystalline structures of PVA and crosslinked PVA. The sharp characteristic peak in the XRD pattern of graphite indicates that it is comprised of many layers, and the interlayer distance of graphite is 3.47 Å ($2\theta = 25.7°$). During oxidation, the graphene sheets were grafted with functional groups, hydroxyl, epoxy, and carboxyl etc., had turned to GO. The interlayer distance of GO increased to 6.91 Å ($2\theta = 12.8°$). Meanwhile, the characteristic peak of GO becomes wide, which indicates that the GO sheets were exfoliated into monolayer or few-layered sheets. However, the distance turned back to 4.72 Å ($2\theta = 18.8°$),

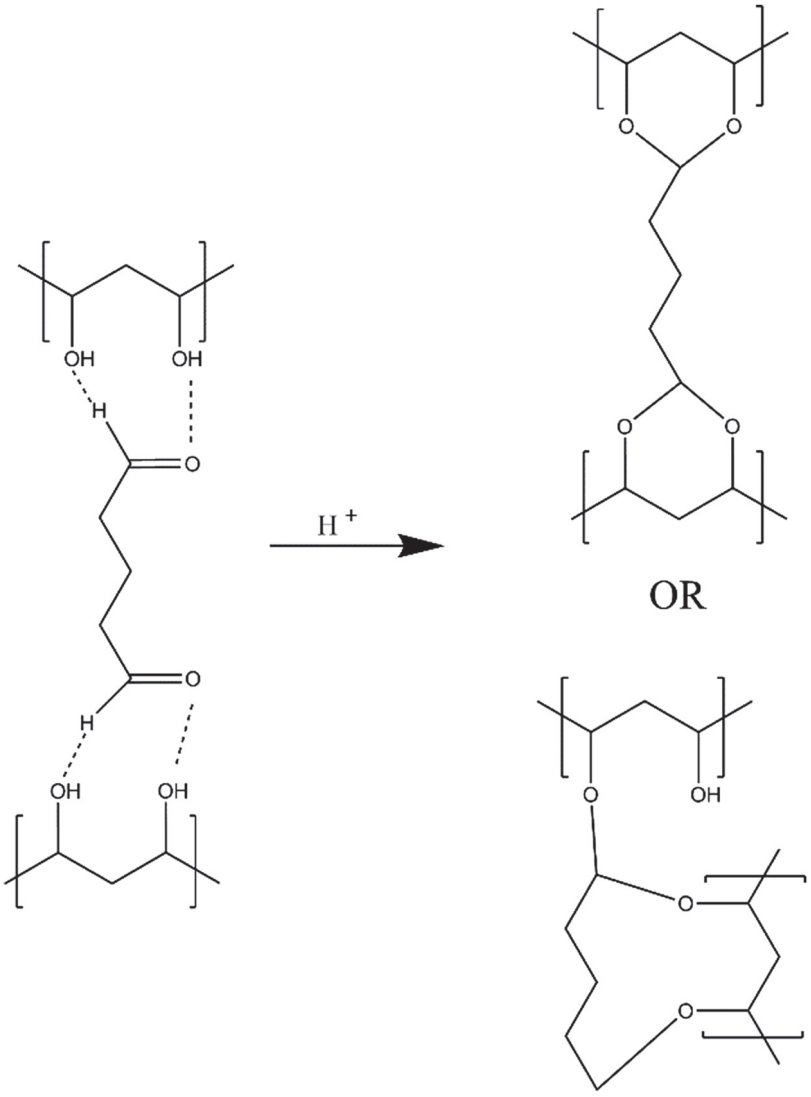

Figure 2: Schematic diagram of PVA crosslinking reaction

indicating most of the oxygen functional groups had been removed, and few few-layered sheets had been restored with the formation of a new structure. On the other hand, the diffraction peak of PVA and crosslinked PVA are shown in the Fig. 3. The intensity of the characteristic peak of PVA become weak after crosslinking, which indicate that the crosslinked chains of PVA were difficult to form the crystalline structures.

Figure 4 shows the color change from transparent yellow film (PVA/GO) to opaque black (PVA/rGO) after reduction. This indicates that PVA matrix was swelled by the reducing agent and the GO within the matrix was reduced successfully to rGO.

Figure 5 shows the SEM images of the fractured surfaces of neat PVA, PVA/GO nanocomposite scaffolds with 5% GO, and PVA/rGO nanocomposite scaffolds with 5% rGO, respectively. The morphology of neat PVA is shown in Fig. 5a. By adding the nanofiller sheets, the surface morphologies of the fractured surfaces of the samples were significantly changed. However, the individual GO and rGO sheets were fully exfoliated and well dispersed in the PVA matrix (as indicated by red arrows in Fig. 5b and c). There was not agglomeration on the GO or rGO fracture surface, indicating the existing interfacial interactions between GO or rGO sheets and PVA chains.

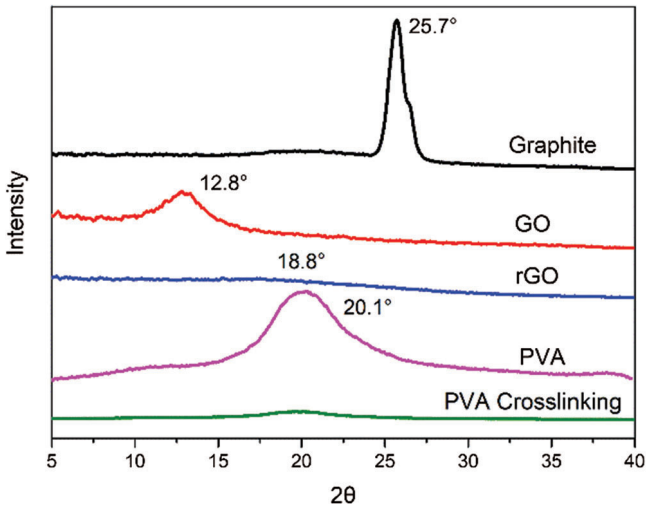

Figure 3: The XRD of graphite, GO, rGO, PVA and crosslinked PVA

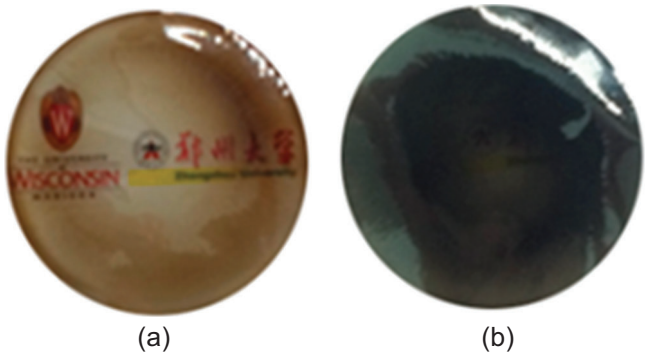

Figure 4: Photographs showing (a) the agglomeration of GO was reduced in water, and (b) the reduction of GO within the PVA matrix after immersion in a reduction agent

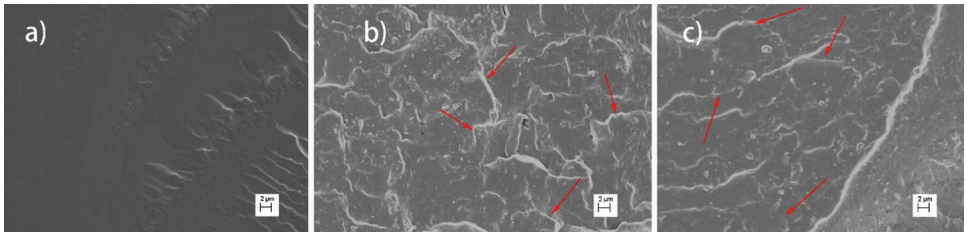

Figure 5: SEM images of the fracture surfaces of (a) neat PVA, (b) PVA/5% GO, and (c) PVA/5% rGO nanocomposite scaffolds

Surface features of the scaffolds are described by contact angles in Fig. 6. The water contact angle can directly indicate the surface wettability of the scaffolds [32-35], which affects protein absorption and subsequent cell adhesion as well as infiltration. Contact angles of graphene-based nanocomposite scaffolds increased with an increase in content of GO and rGO, suggesting that the surface hydrophilicity of the nanocomposite films decreased with the addition of GO or rGO. As shown in Fig. 6, the water contact

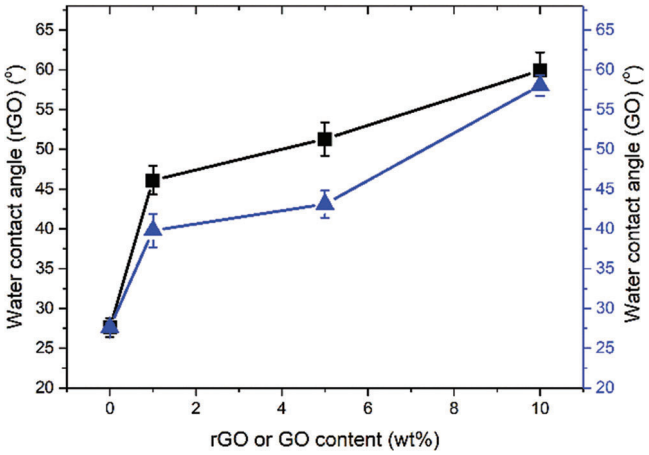

Figure 6: Water contact angles of PVA, PVA/GO, and PVA/rGO nanocomposite scaffolds with various contents of graphene

angle of the PVA/GO nanocomposite regularly increased with increasing the content of GO, from 27.6° for neat PVA to a maximum value of 58° for the PVA/GO nanocomposites with 10 wt% GO an increase of 110%. The water contact angle of the PVA/rGO nanocomposites had a similar trend to the PVA/GO nanocomposite, which was increased to 59.9° by 117% from PVA to a PVA/rGO nanocomposites with 10 wt% rGO. The water contact angle of PVA/rGO nanocomposite is higher than the same proportion of PVA/GO, which is attributed to the better hydrophilic for GO than rGO. The basal planes of GO sheets were heavily decorated with oxygen-containing groups during oxidation, which caused these oxidized layers to become hydrophilic. However, the reduction reaction along with the removal of O-containing functional groups on GO surface could reduce the hydrophilicity of sheets. When GO and rGO were blended into the matrix as a nanofillers, the properties of GO and rGO were introduced to the nanocomposite. The surface property was altered via blending GO or GO nanoparticles with the matrix PVA.

The electrical conductivity of PVA/rGO nanocomposite scaffolds were measured using a four-point probe. It is shown in the Fig. 6 that the electrical conductivity of PVA and PVA/rGO nanocomposite scaffolds with different rGO content. However, the matrix polymer PVA is insulating, the rGO was excellent conductive filler after reduction from GO. One main viewpoint to the conductivity of the PVA/rGO nanocomposite, rGO sheets formed conducting network in the matrix due to the high aspect ratio of rGO sheets. The typical insulating-conductive percolation behavior can be observed with the addition of rGO. Generally, the conductivity remained very low values when the content of rGO was low. However, the conductivity of nanocomposite shown a prominently increase once a critical loading content was achieved and the conducting network was formed [36-40]. As shown in Fig. 7, the electrical conductivity of the PVA/rGO nanocomposite scaffolds increased as the rGO content increased. The electrical conductivity almost remained constant when the rGO content was 1 wt%. Then, an obvious increase of the electrical conductivity of nanocomposite scaffolds from 1 wt% to 5 wt% rGO content was shown, which indicated that the percolation threshold lay between 1 and 5 wt%. The electrical conductivity of the PVA/rGO nanocomposite scaffolds further increased to 12.16×10^{-3} S/m at 10 wt% rGO content.

Figure 8 shows NIH-3T3 fibroblast adhesion on graphene-based nanocomposites and on PVA matrix. The viability of NIH-3T3 cells after incubation on each substrate for 3 days was evaluated using live/dead staining with calcein-AM (to stain live cells with green color) and ethidium homodimer (to stain dead cells with red color). Fluorescence microscopy was used to observe the cells alive or dead by the color. Enhanced NIH-3T3 fibroblast adhesion was also observed on the PVA/rGO nanocomposite scaffolds as compared to the

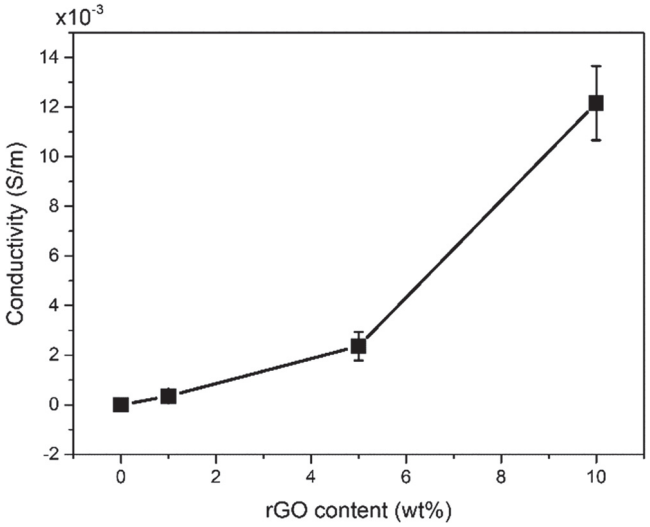

Figure 7: The electrical conductivity of PVA/rGO nanocomposite scaffold as a function of rGO content

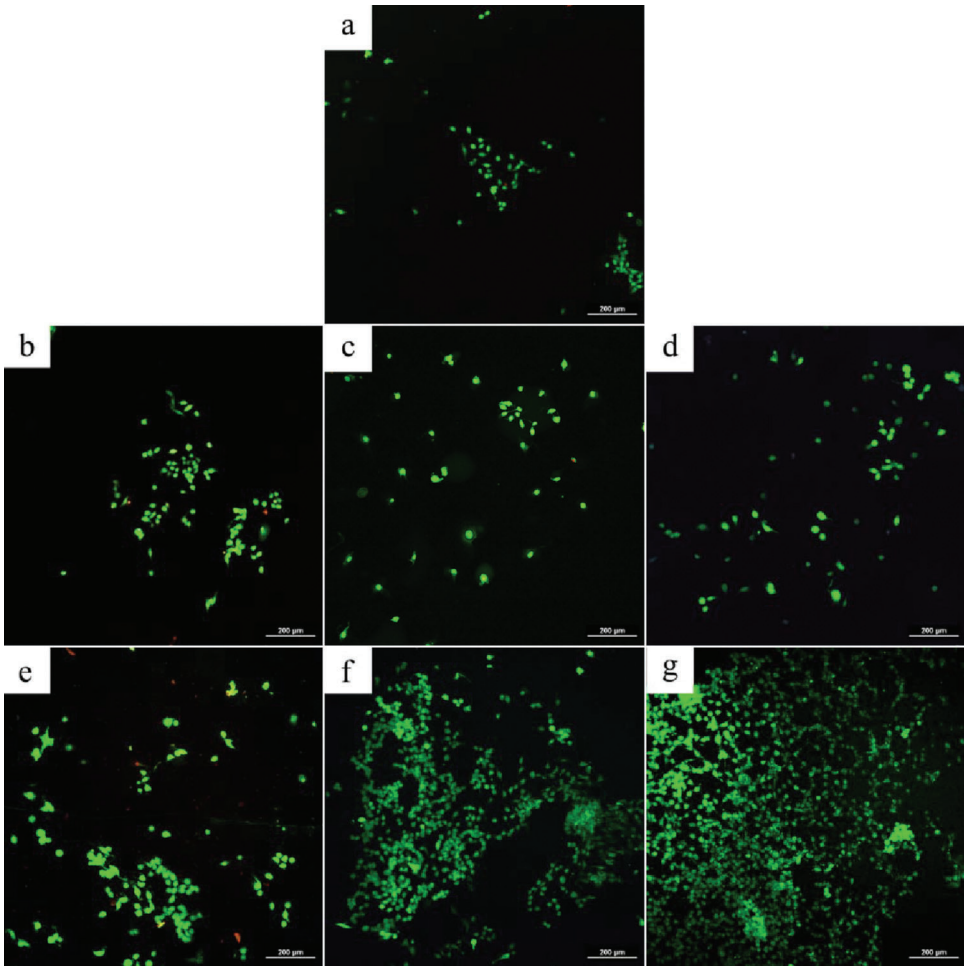

Figure 8: Fluorescence microscope images of NIH-3T3 fibroblasts. Cells were grown on (a) tissue culture PVA, (b) PVA/1 wt% GO, (c) PVA/5 wt% GO, (d) PVA/10 wt% GO, (e) PVA/1 wt% rGO, (f) PVA/5 wt% rGO, and (g) PVA/10 wt% rGO for 3 days. Scale bars are 200 μm

PVA/GO nanocomposite scaffolds. The number of live cells on each substrate can be counted and the result is shown in Fig. 9. As shown in Fig. 9, a small number of cells survived on the PVA scaffold and PVA/GO nanocomposite scaffolds. Furthermore, the number of the alive cell decreased slightly with increasing the content of GO. However, the number of cells obviously increased with the addition of rGO, especially, at 5 wt% and 10 wt% rGO. Especially, the number of cells jumped from 1 wt% to 5 wt% rGO, that was corresponding with the conductivity of PVA/rGO nanocomposite scaffolds. Above showed that GO as a filler had little effect on the cell growth in contrast to rGO. The results indicated that the conductivity of substrate might promote greater initial fibronectin adsorption which strongly correlated with enhanced subsequent cell adhesion.

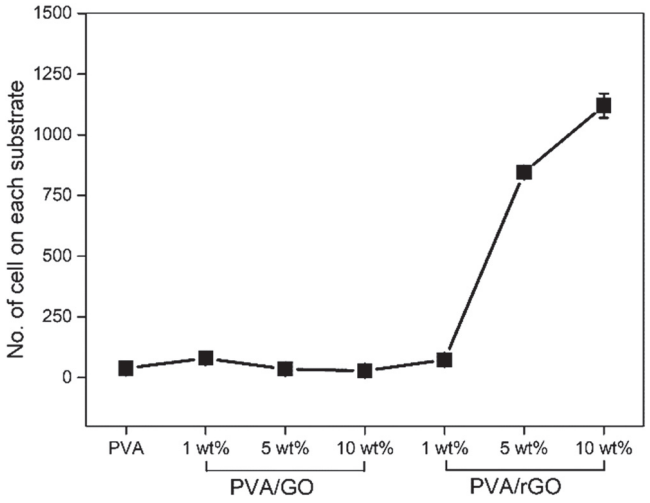

Figure 9: The number of cells on each substrate was evaluated at 3 days

4 Conclusions

In summary, a series of nanocomposite hydrogel scaffolds were made from PVA and graphene lineages by blending. The nanocomposite hydrogel scaffolds emerge conductive zones, with the addition of rGO. The electrical conductivity of the PVA/rGO nanocomposite scaffolds increases to 12.16×10^{-3} S/m at 10 wt% rGO contain. Significantly, the results of cell culture demonstrated that PVA/rGO nanocomposites hydrogel scaffolds could enhance the attachment and the proliferation of NIH-3T3 fibroblasts. Thanks to electrical conductivity of the PVA/rGO hydrogel nanocomposite, the intercellular signaling and cells responses were enabled. Thus, PVA/rGO nanocomposite scaffolds with electrically conductive properties could potentially be potential candidates for tissue engineering applications.

Acknowledgement: This work is financially supported by the Wisconsin Institute for Discovery (WID) at the University of Wisconsin-Madison and the China Scholarship Council.

Conflicts of Interest: The authors declare that they have no conflicts of interest to report regarding the present study.

References

1. Cui, Z., Nelson, B., Peng, Y., Li, K., Pilla, S. et al. (2012). Fabrication and characterization of injection molded poly (ε-caprolactone) and poly (ε-caprolactone)/hydroxyapatite scaffolds for tissue engineering. *Materials Science and Engineering: C, 32(6),* 1674–1681. DOI 10.1016/j.msec.2012.04.064.
2. Ju, J., Peng, X., Huang, K., Li, L., Liu, X. et al. (2019). High-performance porous PLLA-based scaffolds for bone tissue engineering: Preparation, characterization, and in vitro and in vivo evaluation. *Polymer, 180,* 121707. DOI 10.1016/j.polymer.2019.121707.

3. Yang, H., Zhu, Q., Qi, H., Liu, X., Ma, M. et al. (2018). A facile flow-casting production of bioactive glass coatings on porous titanium for bone tissue engineering. *Materials, 11(9),* 1540. DOI 10.3390/ma11091540.
4. Niu, Z., Wang, X., Meng, X., Guo, X., Shen, C. (2019). Controllable fiber orientation and nonlinear elasticity of electrospun nanofibrous small diameter tubular scaffolds for vascular tissue engineering. *Biomedical Materials, 14(3),* 035006. DOI 10.1088/1748-605X/ab07f1.
5. Kumar, A., Han, S. S. (2017). PVA-based hydrogels for tissue engineering: A review. *International Journal of Polymeric Materials and Polymeric Biomaterials, 66(4),* 159–182. DOI 10.1080/00914037.2016.1190930.
6. Hamidi, M., Azadi, A., Rafiei, P. (2008). Hydrogel nanoparticles in drug delivery. *Advanced Drug Delivery Reviews, 60(15),* 1638–1649. DOI 10.1016/j.addr.2008.08.002.
7. Ferreira, L. S., Gerecht, S., Fuller, J., Shieh, H. F., Vunjak-Novakovic, G. et al. (2007). Bioactive hydrogel scaffolds for controllable vascular differentiation of human embryonic stem cells. *Biomaterials, 28(17),* 2706–2717. DOI 10.1016/j.biomaterials.2007.01.021.
8. Ye, M., Mohanty, P., Ghosh, G. (2014). Morphology and properties of poly vinyl alcohol (PVA) scaffolds: Impact of process variables. *Materials Science and Engineering: C, 42,* 289–294. DOI 10.1016/j.msec.2014.05.029.
9. Linh, N. T. B., Lee, B. T. (2012). Electrospinning of polyvinyl alcohol/gelatin nanofiber composites and cross-linking for bone tissue engineering application. *Journal of Biomaterials Applications, 27(3),* 255–266. DOI 10.1177/0885328211401932.
10. Gil-Castell, O., Cervero, R., Teruel-Juanes, R., Badia, J. D., Ribes-Greus, A. (2019). Functionalised poly(vinyl alcohol)/graphene oxide as polymer composite electrolyte membranes. *Journal of Renewable Materials, 7(7),* 655–665. DOI 10.32604/jrm.2019.04401.
11. Branciforti, M. C., Bellani, C. F., Morelli, C. L., Ferrand, A., Benkirane-Jessel, N. et al. (2019). Poly (butylene adipate-co-terephthalate) and poly (ε-caprolactone) and their bionanocomposites with cellulose nanocrystals: thermo-mechanical properties and cell viability study. *Journal of Renewable Materials, 7(3),* 269–277. DOI 10.32604/jrm.2019.01833.
12. Khang, D., Park, G. E., Webster, T. J. (2008). Enhanced chondrocyte densities on carbon nanotube composites: The combined role of nanosurface roughness and electrical stimulation. *Journal of Biomedical Materials Research Part A, 86A(1),* 253–260. DOI 10.1002/jbm.a.31803.
13. He, L. M., Zhao, P. P., Han, Q., Wang, X. Y., Cai, X. et al. (2013). Surface modification of poly-l-lactic acid fibrous scaffolds by a molecular-designed multi-walled carbon nanotube multilayer for enhancing cell interactions. *Carbon, 56,* 224–234.
14. Xia, Y. Q., Wu, H., Tang, D. C., Gao, S., Chen, B. H. et al. (2019). Graphene oxide nanosheet-composited poly (N-isopropylacrylamide) hydrogel for cell sheet recovery. *Macromolecular Research, 27(7),* 679–685. DOI 10.1007/s13233-019-7099-z.
15. Wang, Y., Ji, H., Huang, Z., Zheng, G., Shen, C. (2017). Flexible electrically resistive-type strain sensors based on reduced graphene oxide-decorated electrospun polymer fibrous mats for human motion monitoring. *Carbon, 126,* 360–371. DOI 10.1016/j.carbon.2017.10.034.
16. Jin, L., Hu, B., Li, Z., Li, J., Gao, Y. et al. (2018). Synergistic effects of electrical stimulation and aligned nanofibrous microenvironment on growth behavior of mesenchymal stem cells. *ACS Applied Materials & Interfaces, 10(22),* 18543–18550. DOI 10.1021/acsami.8b04136.
17. Muthuraj, R., Sachan, A., Castro, M., Feller, J. F., Seantier, B. et al. (2018). Vapor and pressure sensors based on cellulose nanofibers and carbon nanotubes aerogel with thermoelectric properties. *Journal of Renewable Materials, 6(3),* 277–287. DOI 10.7569/JRM.2017.634182.
18. Zhang, S., Yang, K., Feng, L., Liu, Z. (2011). In vitro and in vivo behaviors of dextran functionalized graphene. *Carbon, 49(12),* 4040–4049. DOI 10.1016/j.carbon.2011.05.056.
19. Pinto, A. M., Gonçalves, C., Sousa, D. M., Ferreira, A. R., Moreira, J. A. et al. (2016). Smaller particle size and higher oxidation improves biocompatibility of graphene-based materials. *Carbon, 99,* 318–329. DOI 10.1016/j.carbon.2015.11.076.
20. Pinto, A. M., Goncalves, I. C., Magalhaes, F. D. (2013). Graphene-based materials biocompatibility: a review. *Colloids and Surfaces B: Biointerfaces, 111,* 188–202. DOI 10.1016/j.colsurfb.2013.05.022.

21. Rastogi, S. K., Raghavan, G., Yang, G., Cohen-Karni, T. (2017). Effect of graphene on nonneuronal and neuronal cell viability and stress. *Nano Letters, 17(5),* 3297–3301. DOI 10.1021/acs.nanolett.7b01215.
22. Ryoo, S. R., Kim, Y. K., Kim, M. H., Min, D. H. (2010). Behaviors of NIH-3T3 fibroblasts on graphene/carbon nanotubes: proliferation, focal adhesion, and gene transfection studies. *ACS Nano, 4(11),* 6587–6598. DOI 10.1021/nn1018279.
23. Holt, B. D., Wright, Z. M., Arnold, A. M., Sydlik, S. A. (2017). Graphene oxide as a scaffold for bone regeneration. *Wiley Interdisciplinary Reviews: Nanomedicine and Nanobiotechnology, 9(3),* e1437. DOI 10.1002/wnan.1437.
24. Akhavan, O., Ghaderi, E., Akhavan, A. (2012). Size-dependent genotoxicity of graphene nanoplatelets in human stem cells. *Biomaterials, 33(32),* 8017–8025. DOI 10.1016/j.biomaterials.2012.07.040.
25. Syama, S., Aby, C. P., Maekawa, T., Sakthikumar, D., Mohanan, P. V. (2017). Nano-bio compatibility of PEGylated reduced graphene oxide on mesenchymal stem cells. *2D Materials, 4(2),* 025066.
26. Zhou, Y., Jing, X. X., Chen, Y. (2017). Material chemistry of graphene oxide-based nanocomposites for theranostic nanomedicine. *Journal of Materials Chemistry B, 5(32),* 6451–6470. DOI 10.1039/C7TB00680B.
27. Hummers, W. S., Offeman, R. E. (1958). Preparation of graphitic oxide. *Journal of the American Chemical Society, 80(6),* 1339. DOI 10.1021/ja01539a017.
28. Wang, X., Liu, X., Yuan, H., Liu, H., Liu, C. et al. (2018). Non-covalently functionalized graphene strengthened poly(vinyl alcohol). *Materials & Design, 139,* 372–379. DOI 10.1016/j.matdes.2017.11.023.
29. Cote, L. J., Kim, F., Huang, J. (2009). Langmuir–Blodgett assembly of graphite oxide single layers. *Journal of the American Chemical Society, 131(3),* 1043–1049. DOI 10.1021/ja806262m.
30. Marcano, D. C., Kosynkin, D. V., Berlin, J. M., Sinitskii, A., Sun, Z. et al. (2010). Improved synthesis of graphene oxide. *ACS Nano, 4(8),* 4806–4814.
31. Wang, X. F., Salick, M. R., Wang, X. D., Cordie, T., Han, W. J. et al. (2013). Poly(ε-caprolactone) nanofibers with a self-induced nanohybrid shish-kebab structure mimicking collagen fibrils. *Biomacromolecules, 14(10),* 3557–3569. DOI 10.1021/bm400928b.
32. Wang, X., Pan, Y., Liu, X., Liu, H., Li, N. et al. (2019). Facile fabrication of superhydrophobic and eco-friendly poly(lactic acid) foam for oil-water separation via skin peeling. *ACS Applied Materials & Interfaces, 11(15),* 14362–14367. DOI 10.1021/acsami.9b02285.
33. Wang, X., Pan, Y., Shen, C., Liu, C., Liu, X. (2018). Facile thermally impacted water-induced phase separation approach for the fabrication of skin-free thermoplastic polyurethane foam and its recyclable counterpart for oil-water separation. *Macromolecular Rapid Communications, 39(23),* 1800635. DOI 10.1002/marc.201800635.
34. Zhang, X., Wang, X., Liu, X., Lv, C., Wang, Y. et al. (2018). Porous polyethylene bundles with enhanced hydrophobicity and pumping oil-recovery ability via skin-peeling. *ACS Sustainable Chemistry & Engineering, 6(10),* 12580–12585. DOI 10.1021/acssuschemeng.8b03305.
35. Zhang, X., Pan, Y., Gao, Q., Zhao, J., Wang, Y. et al. (2019). Facile fabrication of durable superhydrophobic mesh via candle soot for oil-water separation. *Progress in Organic Coatings, 136,* 105253. DOI 10.1016/j.porgcoat.2019.105253.
36. Liu, X., Li, C., Pan, Y., Schubert, D., Liu, C. (2018). Shear-induced rheological and electrical properties of molten poly(methyl methacrylate)/carbon black nanocomposites. *Composites Part B: Engineering, 164,* 37–44. DOI 10.1016/j.compositesb.2018.11.054.
37. Pan, Y., Liu, X., Kaschta, J., Hao, X., Liu, C. et al. (2017). Viscoelastic and electrical behavior of poly(methyl methacrylate)/carbon black composites prior to and after annealing. *Polymer, 113,* 34–38. DOI 10.1016/j.polymer.2017.02.050.
38. Liu, X., Pan, Y., Zheng, G., Schubert, D. W. (2016). Rheological and electrical behavior of poly(methyl methacrylate)/carbon black composites as investigated by creep recovery in shear. *Composites Science and Technology, 128,* 1–7. DOI 10.1016/j.compscitech.2016.03.011.
39. Liu, X., Pan, Y., Hao, X., Dai, K., Schubert, D. W. (2016). The role of conductive pathways in the conductivity and rheological behavior of poly(methyl methacrylate)-graphite composites. *Journal of Applied Polymer Science, 133(32),* 43810.
40. Liu, X., Krückel, J., Zheng, G., Schubert, D. W. (2013). Mapping the electrical conductivity of poly(methyl methacrylate)/carbon black composites prior to and after shear. *ACS Applied Materials & Interfaces, 5(18),* 8857–8860. DOI 10.1021/am4031517.